



# TEMPO-oxidized Cellulose Nanofibers/ Alginate Nanocomposite as a Promising nanocomposite Material for the Adsorption of Cationic Dyes

Ragab Abouzeid<sup>1,2</sup> · Mohamed Taha<sup>3</sup> · Ramzi Khiari<sup>4,5,6</sup> · Qinglin Wu<sup>1</sup>

Received: 7 February 2023 / Accepted: 21 March 2023 / Published online: 5 April 2023

© This is a U.S. Government work and not under copyright protection in the US; foreign copyright protection may apply 2023

## Abstract

TEMPO-oxidized cellulose nanofiber/alginate nanocomposite (T-CNF/SA) was prepared and characterized as a recyclable adsorbent for cationic dye. TEMPO-oxidized CNFs contain a large number of carboxylic groups, they may interact with methylene blue as a model of cationic dye in aqueous solutions. Two materials were synthesized in this study: T-CNF and CNF/SA nanocomposite. In order to determine the ability of the nanocomposite to remove the dye, batch sorption experiments were performed using the nanocomposite after their synthesis and characterization. In the studied concentration range of dye, equilibrium data were well fitted to the Langmuir isotherm model, indicating that dye removal is a favorable process. At 25 °C and neutral pH, the maximum adsorption capacities reached 185.2 mg dye/g and 216.4 mg dye/g for T-CNF and for T-CNF/SA, respectively. The adsorption efficiency was up to 95% after 2 h for T-CNF/SA. The adsorption data fitted well with the second-order kinetic model high correlation coefficients ( $R^2 > 0.99$ ) and the isotherm data followed the Langmuir model equation. Finally, the study presents a feasible, practical, and reusable nanocomposite as an interesting adsorbent for wastewater treatment.

**Keywords** Cellulose nanofiber · Nanocellulose · Sodium alginate · Cationic dye · Adsorption

## 1 Introduction

Our planet is distinctly endowed with the elements that are needed for the support of life to exist, including water, an essential component of life on earth. However, most of the water on the planet is contained in oceans, seas, and saline groundwaters, which make up approximately 97% of all the water on the planet. In other words, only 2.5–2.75% of the water is fresh, out of which 1.75–2% is frozen in glaciers, ice, and snow. Fresh groundwater makes up approximately 0.5–0.75% of all water on earth, and lakes, swamps, rivers, and streams make up less than 0.01%. The majority of this 0.01% are located in Africa (34), followed by 26% in Russia, 25% in North America, and the remainder in other lakes scattered across the Earth's surface [1]. According to the Environmental Protection Agency (EPA), contaminants in wastewater from many industries include heavy metals, organic dyes, oils, and other toxic pollutants which can have negative effects on both human health and the environment [2]. In the natural environment, most of these wastes are stable and non-degradable. It is important to protect water sources by forming heavy metals and organic-colored materials (dyes) from industrial waste effluents. In addition, the

✉ Ragab Abouzeid  
r\_abouzeid2002@yahoo.com

✉ Qinglin Wu  
QWu@agcenter.lsu.edu

<sup>1</sup> School of Renewable Natural Resources, Louisiana State University AgCenter, Baton Rouge, LA 70803, USA

<sup>2</sup> Cellulose and Paper Department, National Research Centre, Dokki, Giza, 12622, Egypt

<sup>3</sup> Mechanical Engineering Department, College of Engineering and Technology, Arab Academy of Science, Technology and Maritime Transport, Sadat Road, P.O. Box 11, Aswan, Egypt

<sup>4</sup> Faculty of Sciences of Monastir, Laboratory of Environmental Chemistry and Clean Process (LCE2P-LR21ES04), University of Monastir, Monastir 5019, Tunisia

<sup>5</sup> Department of Textile, Higher Institute of Technological Studies of Ksar Hellal, Ksar Hellal, Tunisia

<sup>6</sup> Univ. Grenoble Alpes, CNRS, Grenoble INP, LGP2, Grenoble F-38000, France

shortage of water resources due to population growth is considered a critical issue, especially with an increasing demand for pure water [3, 4]. In order to reduce heavy metals and/or dyes from water, many strategies have been developed for water purification based on precipitation with chemicals [5], ion-exchange biological treatment [6], photocatalytic degradation [7], membrane filtration and adsorption [8–10], coagulation/flocculation [11] and electrodialysis [12]. It is recommended that the adsorption method is preferred over the other methods because it is a low cost, high efficacy, eco-friendly, wide range, and readily available method. [13]. There has been an increase in the use of eco-friendly and sustainable polysaccharides for water treatment [14, 15]. As adsorbents for various pollutants, cellulose nanomaterials (CNMs) are a new aspect to attract more attention. CNMs have renewability, biodegradability, abundance, renewability, high surface area, good mechanical properties and low cost [16–23]. The use of CNMs based systems for decontamination water of heavy metals and organic dyes have been reported [24–26]. Sodium alginate (SA) is a biopolymer with two monosaccharide units namely:  $\alpha$ -l-guluronic acid and  $\beta$ -d-mannuronic acid or their copolymers in varying proportions attached with (1→4)-linked [16, 27, 28]. SA gels have been used to form homogenous, permeable spheres entrapped in gel matrixes for the removal of dyes from wastewater [29–32]. The TEMPO-oxidized CNFs have excellent mechanical properties, high specific surfaces, and can be chemically modified for a variety of applications. Surface characteristics facilitate the availability of COO– groups, either in their acid or salt form. Additionally, a wide range of CNF-based products can be produced, such as aerogels, nanopapers, and hydrogels [33, 34]. This study aims to develop polymer structures based on alginate and T-CNF that can remove cationic dye from aqueous solutions. As part of this experiment, T-CNF/alginate nanocomposite containing 50% of T-CNF were prepared and subjected to batch experiments with dye concentrations. T-CNFs was treated the same way. To conclude, the present work investigates In addition to the adsorption kinetics and the isotherm were studied. The possibility of using environmentally friendly, renewable, and biodegradable CNMs to decontaminate the wastewater will have significant impact on the economy of developing countries where water contamination is turning into a significant natural issue.

## 2 Experimental

### 2.1 Materials

Bleached bagasse pulp was produced by the Qena Company (pulp and paper, Qena, Egypt) and it used to produce

CNMs. TEMPO (2,2,6,6-tetramethylpiperidine 1-oxyl radical), Sodium alginate and calcium chloride ( $\text{CaCl}_2$ ) of laboratory grade were also purchased from Sigma-Aldrich. sodium hypochlorite solution and sodium bromide were purchased from Sigma-Aldrich, France. All the used chemical products were purchased and utilized as received from Sigma-Aldrich.

### 2.2 TEMPO-cellulose Nanofiber Preparation

The bleached bagasse pulp was oxidized by using TEMPO agent according to the method described by Saito et al. [35]. Briefly, 25 gm of bleached fibers were dispersed in 2.5 L of distilled water for 30 min. with mechanical stirring. After, 0.4 g of TEMPO and 4 g of sodium bromide, followed by 250 mL of 15% sodium hypochlorite solution, stirring continuously, keeping the pH from 10 to 10.5 using NaOH (0.1 M) until no pH variation was observed. After that, HCl (0.1 M) was used to adjust the pH to neutral. After oxidation, the fibers were filtered and washed with distilled water. The Masuko grinder was used to homogenize suspensions of oxidized fibers at 2% consistency. This means that the suspension contained 2% by weight of fibers and 98% water. The oxidized fibers are likely to be chemically treated fibers that have undergone an oxidation process to increase their reactivity and make them easier to bond with other fibers or materials. The carboxyl content was determined by conductimetric titration in order to assess the effectiveness of the TEMPO-mediated oxidation of fibers [36]. In brief, dry sample (50 mg) was suspended in 15 mL of 0.01 M HCl for 2 h., for exchanging  $\text{Na}^+$  cations with  $\text{H}^+$  protons. Titrated with 0.01 M NaOH solution and the conductivity was recorded every 0.5 mL of NaOH. Based on the sudden change in conductivity, we determined the carboxylate content of T-CNF. A carboxylate content, CC (mmol/g), was calculated using Eq. (1):

$$CC = \left( \frac{V_2 - V_1}{m} \right) \times N(\text{NaOH}) \quad (1)$$

where  $V_1$  and  $V_2$  correspond to the volumes of NaOH solution (mL) used from neutralizing the added HCl and carboxylic acid on the T-CNF.  $N(\text{NaOH})$  corresponds to the of NaOH concentration solution (M), and  $m$  is the weight of the dried sample (g).

### 2.3 Preparation of TCNF/SA Nanocomposite

T-CNF gel in water suspension was used with dry solid content of 2%. SA in powder form was directly mixed with T-CNF with vigorously mixing for 2 h to generate a homogeneous dispersion. After that crosslinking with aqueous

solutions of calcium chloride (0.3%) was carried out and the formed hydrogel was freeze-dried for further use.

## 2.4 Characterization of T-CNF/SA Nanocomposite

Scanning electron microscopy analysis (SEM) (FEI-Quanta 200 FEG -ESEM, Eindhoven, Netherlands) was used to characterize the morphological properties of the prepared samples. T-CNF studied using an Atomic Force Microscope (AFM) Multimode (Veeco NanoScope-V, Canada) in trapping mode with multi 130 tips. The FT-IR spectra (Fourier Infrared Spectra) were acquired with a Perkin Elmer FT-IR spectrometer (Perkin Elmer, USA) and KBr tablets in the range 4000–500  $\text{cm}^{-1}$ . The viscosity measurements in a plate-cone configuration were done using the rotational physical MCR 301 rotational rheometer from Anton Paar (Germany). Precisely, the parallel plates with a diameter of 25 mm and a gap distance of 1 mm were used. During the measurements, the temperature was kept at 23 °C. The shear rate ranged between  $10^{-3}$  and  $10^3 \text{ s}^{-1}$ . Zeta potential and the point of zero charge (pHzpc) were determined using a Nicomp 380 ZLS dynamic light dissipating (DLS) instrument (PSS, Santa Barbara, CA, USA). X-ray diffraction pattern was established using (XRD, X-ray diffractometer (PANalytical, Eindhoven Netherlands) at room temperature with monochromatic Cu K ( $= 1.5418 \text{ \AA}$ ) radiation at 4° to 60°.

A thermogravimetric analysis (TGA) (Q50, TA Instruments Inc., New Castle, DE) were used to study the thermal stability of synthesized nanocomposites. In this test, temperatures ranged from 30 to 800 °C, heating rates of 10 °C/min, and the sample weight was less than 5 mg.

## 2.5 Adsorption Kinetics

The adsorption performance experiment was conducted by stirring 50 mg of T-CNF and T-CNF/SA freeze dried materials with 100 mL of MB dye for two hours. The experiments were conducted at a neutral pH and room temperature. An UNICO UV-2000 spectrophotometer was used to estimate the dye concentration at the beginning and end of the experiment. The absorption capacity was calculated using the following equation.

$$q_e = \left( \frac{C_o - C_e}{W} \right) V \quad (2)$$

where  $w$  is the weight of the dried nanocomposite (g), and  $V$  (L) is the volume of dye solution.  $C_o$ , and  $C_e$  is the dye concentration before and after adsorption ( $\text{mg.L}^{-1}$ ),  $q_e$  is the amount of dye adsorbed ( $\text{mg.g}^{-1}$ ).

The adsorption kinetic dye adsorption was studied using different dye concentrations ranging from (50 to 800  $\text{mg.L}^{-1}$ ) for 3 h. Each experiment contained 50 mg of T-CNF/SA dried nanocomposite in dye solutions. The adsorbed dye ( $q_e$ ) was then plotted against time ( $t$ ) and examined utilizing different models to get the kinetic parameters of adsorption.

For the evaluation of regeneration efficiency and cost effectiveness, the T-CNF-SA nanocomposites were used for five consecutive cycles of adsorption-desorption. 10 mg of adsorbent were dispersed into 10 mL of 0.1 M  $\text{HNO}_3$  solution after adsorption, resulting in the desorption of MB from the nanocomposite.

$$\text{Adsorption efficiency\%} = \frac{CV}{q_e M} \quad (3)$$

where  $M$  is the adsorbent mass in gram,  $C$  is the concentration in the desorption solution,  $V$  (L) is the desorption volume, and  $q_e$  the adsorbed amount of MB.

## 3 Result and Discussion

### 3.1 Characteristics of the Prepared Nanocomposite

AFM was used to characterize the morphology of T-CNF and T-CNF/SA prepared (Fig. 1(A, B)). According to Fig. 1A, T-CNF has a diameter range of 10 to 20 nm and a length of in the micrometer range, which is confirmed by the distribution of the diameter measurements (Fig. 1A\*). As a result of the formation of carboxylate groups on its surface, T-CNF displays a uniform structure, which is in agreement with our previous work [37]. The Conductivity titration method was used to evaluate the surface carboxylate content of TEMPO-oxidized cellulose nanofibers which was estimated to be 1.06 mmol. The AFM of T-CNF/SA nanocomposite is shown in Fig. 1(B). It can be seen from the micrograph that the cellulose nanofibers are homogeneous distributed within the alginate gel. Cellulose nanofibers and alginate did not separate into phases, indicating a good interaction between them. The XRD spectra of T-CNF and T-CNF/SA shown in the Fig. 1 (C). The original diffraction pattern of T-CNF exhibited the typical peaks characteristic of native cellulose which could be indexed to (110) and (200) planes. However, XRD spectrum of T-CNF/SA still shows characteristic cellulose peaks as a result of the ionic cross-linking reaction of amorphous alginate and T-CNF. Figure 1(D) shows the FTIR spectra of T-CNF and T-CNF/SA. There are peaks at 3500 and 3400  $\text{cm}^{-1}$  for O-H stretching vibration for T-CNF and T-CNF/SA, respectively. T-CNF/SA and T-CNF/A both exhibit asymmetric and symmetrical absorption bands of  $\text{COO}^-$  at 1638, 1435  $\text{cm}^{-1}$ , and

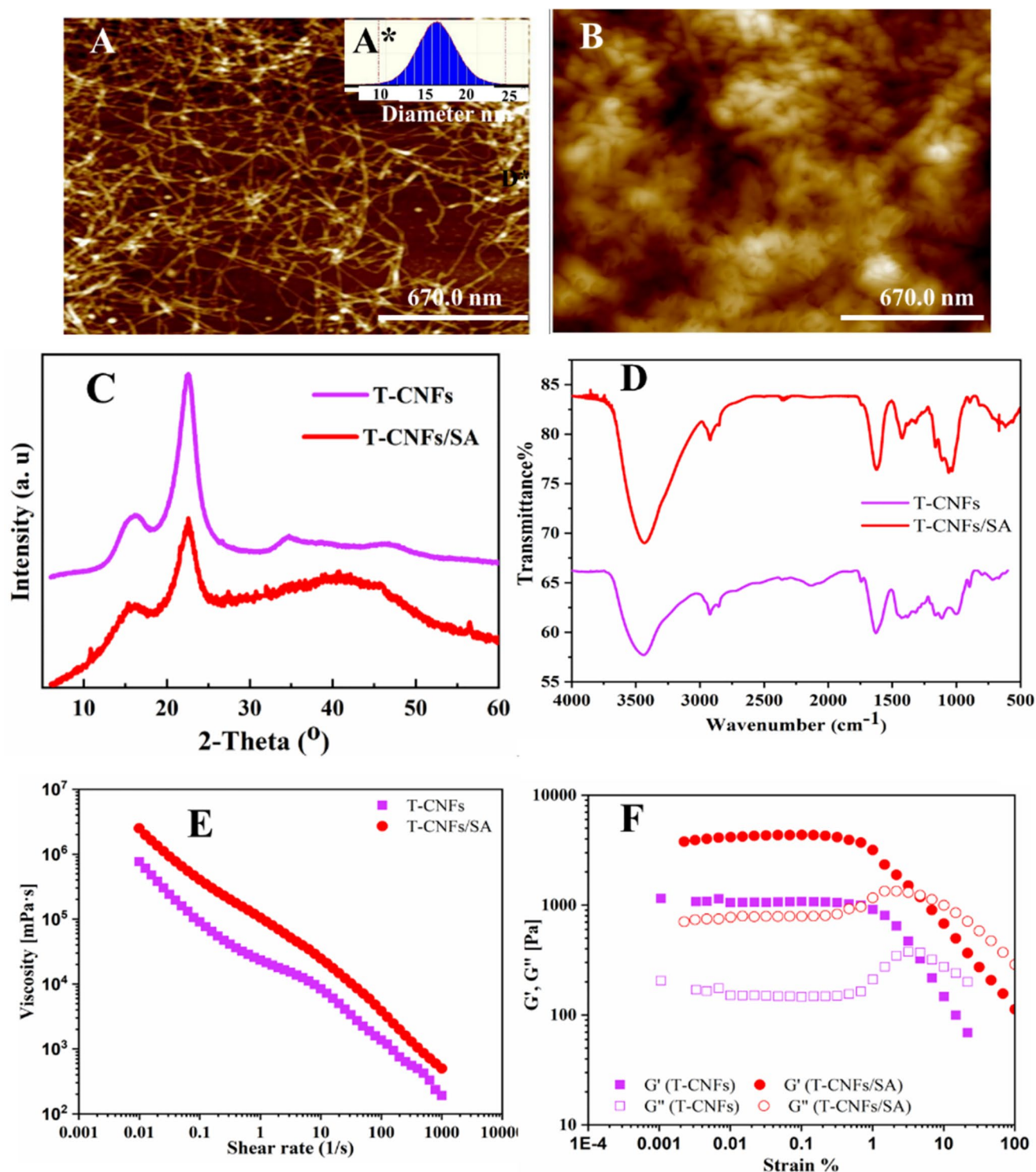


**Fig. 1** (A, B) AFM, (C) XRD, (D) FTIR of T-CNF and T-CNF/SA (E) Viscosity vs. shear rate and (F) strain sweep at 1 Hz: evolution of the storage modulus  $G'$  and loss modulus  $G''$  for T-CNF and T-CNF/SA nanocomposites

1618, 1428  $\text{cm}^{-1}$ , respectively. This shift, which occurs for symmetrical deformation of the COO – group is evidence of the ionic crosslinking of the carboxylate groups [38–40].

T-CNF and T-CNF/SA nanocomposites were also characterized in terms of rheological properties (Fig. 1 (E)). The viscosity as a function of shear rate from 0.01 to 1000  $\text{s}^{-1}$  was studied. The viscosity measurement gives insight into

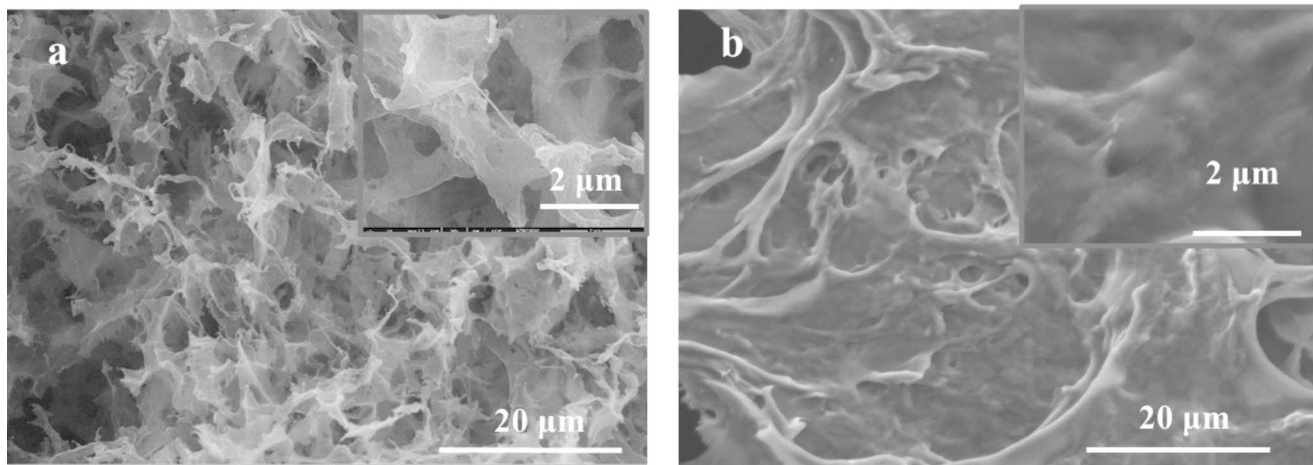


**Fig. 2** (A, B) SEM of T-CNF and TCNFs/SA.

the variation in flow behavior influenced by yield stress, consistency, homogeneity, and overall nanocomposite quality. For both samples, shear-thinning was observed. As a result of the formation of cellulose nanofiber and alginate networks, the viscosity of T-CNF/SA is greater than that of T-CNF, increasing resistance to shear. Moreover, viscosity decreases significantly as the shear rate increases, which is a classic characteristic of a non-Newtonian fluid. [41, 42] The decrease in flow resistance occurs as the nanocomposite network weakens due to increased shear rate, releasing the trapped liquid within. This results in a decreased apparent viscosity. At a frequency of 1 Hz, strain amplitude was determined for T-CNF and T-CNF/SA (Fig. 1F). The storage modulus ( $G'$ ) and loss modulus ( $G''$ ) at low strains are independent of strain amplitudes, and  $G' > G''$ , indicating highly structured material. Higher strains result in a drop in  $G'$ , indicating structural deformation and a change in the nanocomposite's behavior from elastic to viscous (the loss modulus  $G''$  increases). The surface morphology of both T-CNF and T-CNF/SA nanocomposite was displayed in Fig. 2 (A and B), respectively. Figure 2. (a, b) illustrates a smooth cell structure with homogeneous distribution of T-CNF with SA, and no aggregates of T-CNF are found. T-CNF and SA interact strongly, and the crosslinking with  $\text{Ca}^{2+}$  also contributes to the homogeneity. Also, it can be noticed that the negative charges on the nanocomposite surface were increased which confirmed with zeta potential measurements. These results are consistent with those previously mentioned works [43, 44]. The zeta potential of T-CNF and T-CNF/SA at neutral pH were found to be  $-42.5$  and  $-54.0$  mV respectively. The value of zeta potentials for the two samples were negatively charged with higher recorded value for T-CNF/SA nanocomposite. These observations confirm again that the expected higher adsorption capacity of T-CNF/SA for the cationic dyes (MB) comparing to T-CNF alone. This high

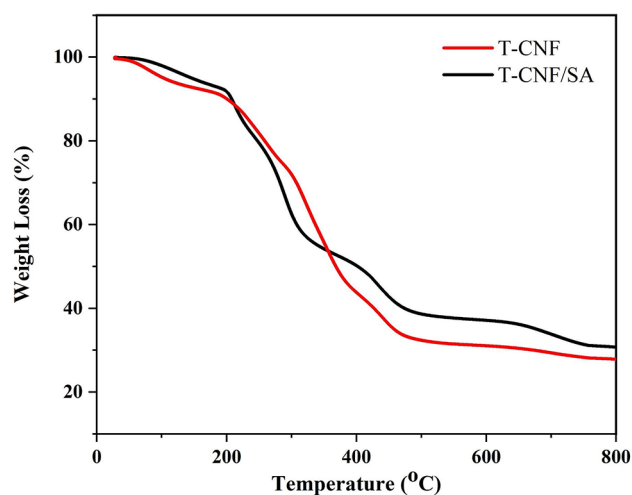


**Fig. 3** TGA of T-CNF and T-CNF/SA nanocomposites

adsorption capacity originated from the electrostatic attractions and complexation of T-CNF/SA nanocomposite and the cationic dyes.

### 3.2 Thermogravimetric Analysis (TGA)

Thermogravimetric analysis (TGA) is a useful tool for investigating the thermal stability and decomposition behavior of materials. In this case, TGA was used to study the prepared nanocomposites, TCNF and TCNF/SA. Figure 3 displays the TGA plots obtained for these materials under  $\text{N}_2$  gas. The TGA results revealed that both materials underwent a first degradation step between 50 and 200 °C, which was attributed to the evaporation of residual water. This initial weight loss accounted for approximately 15% for both TCNF and TCNF/SA. At higher temperatures, the thermal decomposition of both materials was observed in the form of a second degradation step. The primary weight

loss occurred between 250 and 350 °C, followed by a relatively slow decrease between 350 and 450 °C, which was caused by the degradation of pyranose rings present in the TCNF backbone. The final degradation steps were observed at 500 to 800 °C, leading to a final residue of 22% and 28% for TCNF and TCNF/SA, respectively. The TGA results provide valuable information on the thermal stability of the materials and can be used to determine the optimal processing conditions for these nanocomposites.

### 3.3 Adsorption Study

#### 3.3.1 MB Adsorption at Different pH

In dye adsorption, pH affects the surface properties of the absorbent and the degree of ionization of dyes (Fig. 3A). The T-CNF and T-CNF/SA gels become deprotonated when the pH increase (alkaline medium), which increases cationic dyes' adsorption capacity. In addition, due to competing with cationic dye atoms, a solution with H<sup>+</sup> ions can be also interacting with targets outside all samples. Neatly, the T-CNF and T-CNF/SA MB adsorption limits decrease at low pH for these routes because fewer dynamic adsorption areas exist. By calculating the zero-point charge (ZPC) of the nanocomposites. ZPC for T-CNF/SA hydrogel, it is possible to predict the optimal pH range for the adsorption of dyes. The ZPC of the T-CNF and T-CNF/SA nanocomposites is found to be at a pH of 4.3 and 4.1 respectively. At a pH below the ZPC, the surface of the nanocomposite is positively charged, and therefore, it can attract negatively charged dye molecules. Conversely, at a pH above the ZPC, the surface of the nanocomposite is negatively charged, and it can attract positively charged dye molecules.

#### 3.3.2 Contact Time Effect Into Adsorption and Adsorption Kinetics

The adsorption time of contact is a significant parameter that is used to determine the related properties [45]. Figure 4B illustrates the recorded values of MB dye adsorption capacity on T-CNF and T-CNF/SA as a function of adsorption time. T-CNF and T-CNF/SA both exhibited high adsorption rates in the first 60 min., with equilibrium reached after 60 to 120 min. Due to the concentration difference between the dye solution and the solid-liquid interface, which acts as a driving force, the adsorption is significant at first. Compared to pure T-CNF, T-CNF/SA nanocomposite has a higher potential for adsorption. The high concentration of carboxylate ions in the nanocomposite, which has previously been validated by Zeta potential studies, may be the cause of the quick electrostatic attraction with cationic MB. A pseudo-first-order kinetic model and a pseudo-second-order kinetic

model Fig. 4(C, D) respectively, were applied to examine the MB adsorption mechanism. The kinetic parameters corresponding to these models are recapitulated in Table 1. The kinetic data were established and studied using the pseudo-first order and pseudo-second-order kinetic models. From the Eqs. 4 and 5, It can be determinate the complex interaction between an adsorbent and an adsorbate:

$$\text{Log}(q_e - q_t) = \text{Log}(q_e) - \frac{K_1}{2.303}t \quad (4)$$

$$\frac{t}{q_e} = \left( \frac{t}{q_e} + \frac{1}{K_2 q_e^2} \right) \quad (5)$$

Where  $q_t$  (mg.g<sup>-1</sup>) and  $q_e$  (mg.g<sup>-1</sup>) represents the adsorption at time  $t$  (min.) and adsorption at equilibrium, respectively.  $k_1$  (min.<sup>-1</sup>) and  $k_2$  (g mg<sup>-1</sup> min.<sup>-1</sup>) is the rate constant for pseudo-first-order and pseudo-second-order, respectively.

From the Fig. 4, the first- and second-order kinetic models and the obtained data in Table 1, different conclusions can be announced. Based on the results, it can observe that a pseudo-second-order kinetic model accurately very well the representation of the adsorption mechanism. For all ranges of contact times (Fig. 4B), fittings of the first-order kinetic function (Eq. 4) were not very satisfactory. For T-CNF and T-CNF/SA, the pseudo-first-order model correlation coefficients were 0.85 and 0.84, respectively. Furthermore, the equilibrium adsorptive values ( $q_e$  cal) differed greatly from the experimental data ( $q_e$  exp.). This suggests that the pseudo-first-order equation was not accurate for the adsorption system [46, 47]. According to the pseudo-second-order adsorption kinetics data, adsorption occurs via a biatomic adsorption mechanism with the nanocomposite and MB dyes functional groups participating in the rate-determining step of adsorption [48, 49]. A pseudo-second-order model was fit to adsorption kinetic data for T-CNF and T-CNF/SA (Fig. 4D) with correlation coefficients ( $R^2=0.99$  for T-CNF and T-CNF/SA) that are higher than those for pseudo-first order ( $R^2 \sim 0.85$  and  $0.84$  for T-CNF and T-CNF/SA, respectively). The experimental adsorption ( $q_e$ ,exp) and calculated results ( $q_e$ . calc) of the pseudo-second-order kinetic model were similar as well.

### 3.4 Adsorption Isotherms

To define the adsorption processes, adsorption isotherms are used, commonly for the adsorbed amount on the nanocomposite 's surface. A combination of Langmuir Eqs. 6 and 7 was used to assess the T-CNF and T-CNF/SA isotherm information.

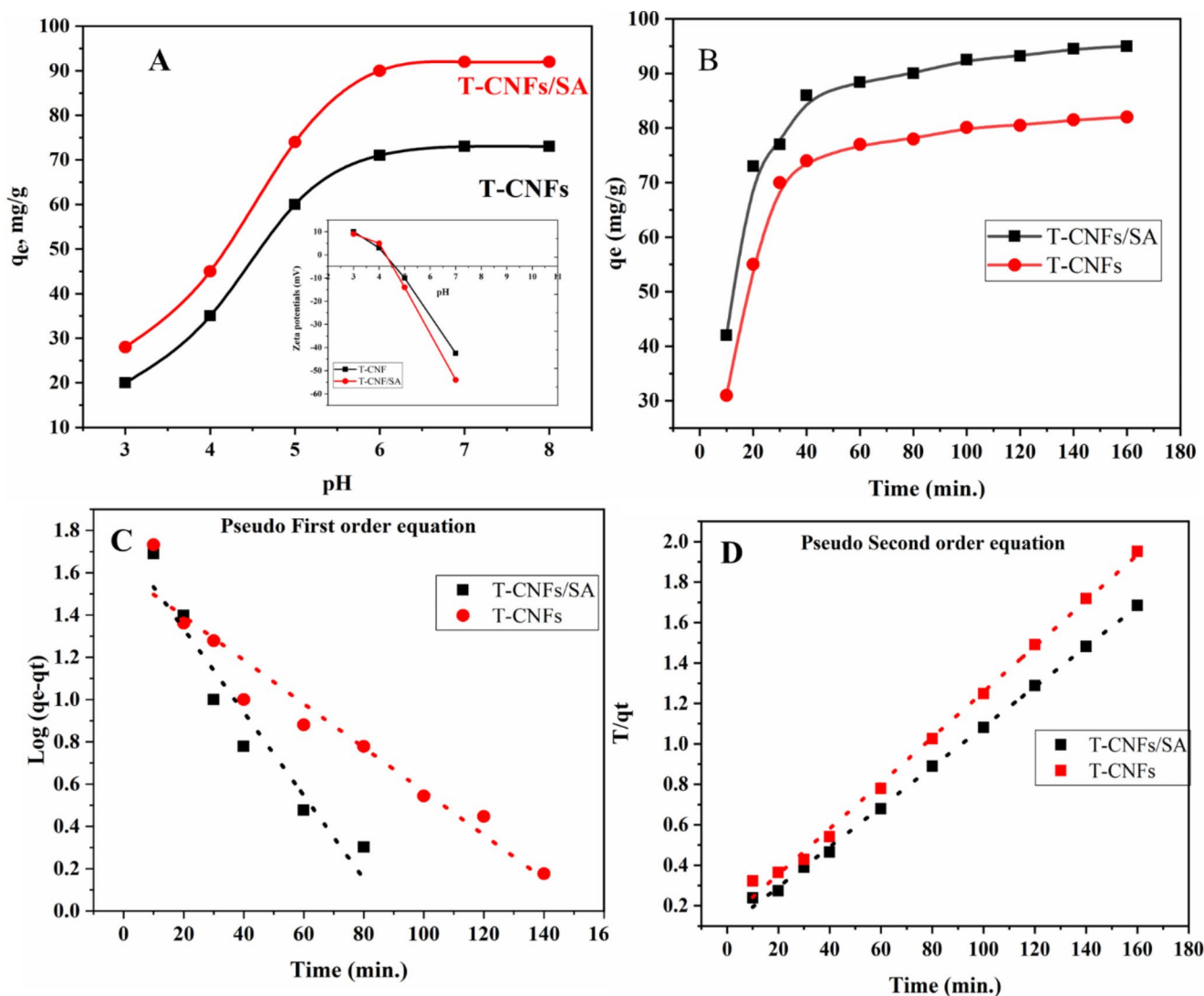


**Fig. 4** (A) Effect of pH values on the adsorption capacities of T-CNF and T-CNF/SA, (B) non-linear fitting for MB adsorption of adsorption kinetic curves (C) linear fitting of the pseudo first order kinetic model

for MB adsorption, and (D) linear fitting of the pseudo second order kinetic model for MB adsorption

**Table 1** Kinetic parameters for MB adsorption by T-CNF and T-CNF/SA nanocomposites

	Pseudo first order parameters				Pseudo second order parameters		
	$q_{e,exp}$ (mg.g <sup>-1</sup> )	$q_{e,cal}$ (mg.g <sup>-1</sup> )	$K_1$ (min. <sup>-1</sup> )	$R^2$	$q_{e,cal}$ (mg.g <sup>-1</sup> )	$K_2$ (min.) <sup>-1</sup>	$R^2$
T-CNF	82	48	0.033	0.853	89.28	$9.68 \times 10^{-4}$	0.99
T-CNF/SA	91.8	35	0.028	0.849	97.08	$1.3 \times 10^{-3}$	0.99

$$\frac{C_e}{q_e} = \frac{1}{K_L q_{max}} + \frac{C_e}{q_{max}} \quad (6)$$

In this equation,  $q_e$  indicates the amount of MB adsorbed by the nanocomposite (mg.g<sup>-1</sup>),  $C_e$  represents the equilibrium dye concentration (mg.L<sup>-1</sup>),  $q_{max}$  represents the maximum number of MB adsorbed on the nanocomposite (mg.g<sup>-1</sup>), and  $K_L$  indicates the Langmuir constant (mg/l).

The Freundlich equation is given by:

$$\log q_e = \frac{1}{n} \log C_e + \log P \quad (7)$$

where  $P$  represents the adsorption capacity (mg.g<sup>-1</sup>), and  $n$  is a constant representing the adsorption intensity (dimensionless).

Figure 5 shows the isotherms of adsorption at various MB dye initial concentrations (ranging from 50 to 800 mg.L<sup>-1</sup>). The parameters for fitting the Langmuir and

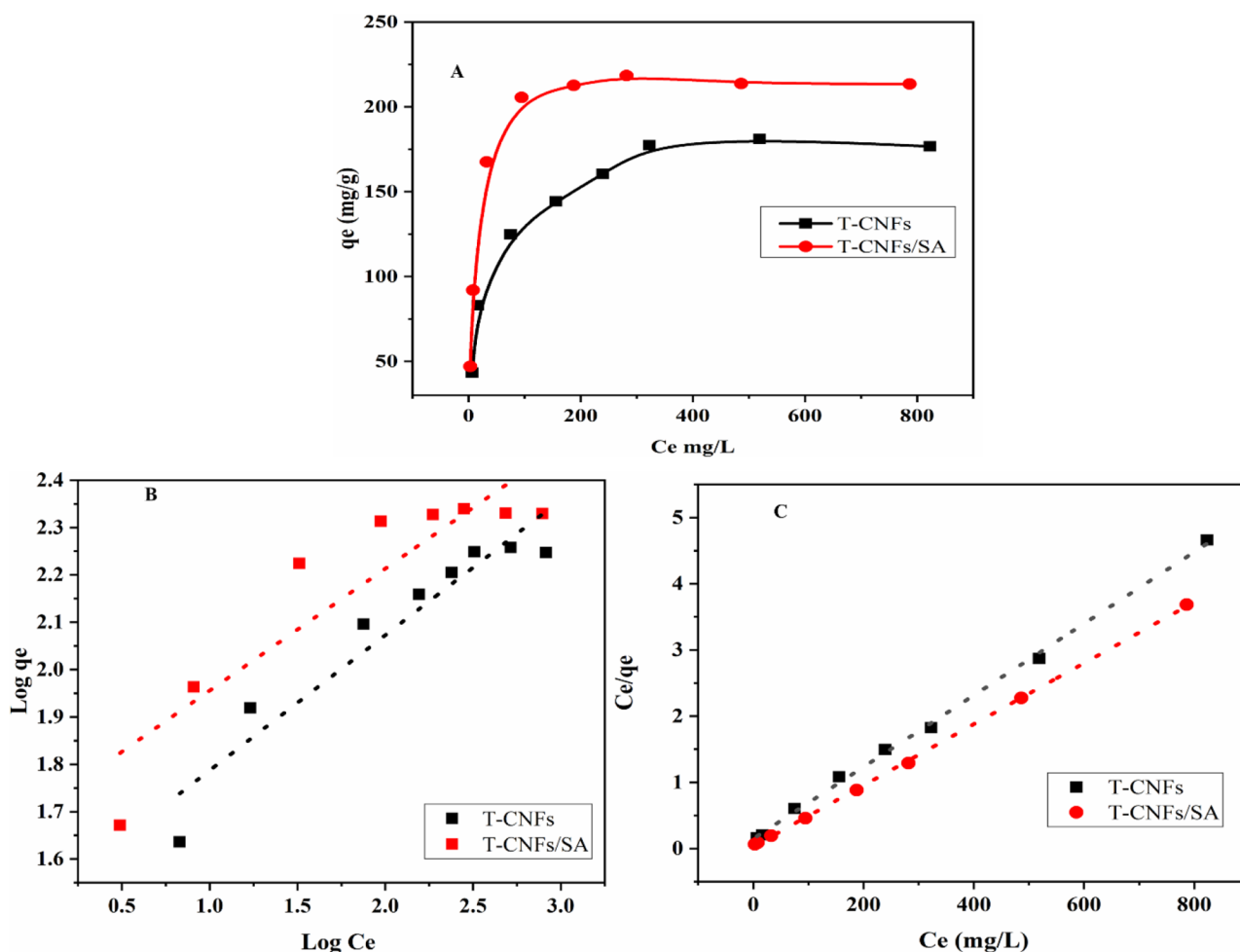


**Fig. 5** MB dye adsorption isothermal curves: **(A)** Nonlinear fit of MB adsorption, **(B)** MB adsorption model fitted linearly (Langmuir model) **(C)** and Freundlich model

**Table 2** MB adsorption parameters for different equilibrium models of T-CNF and T-CNF/SA.

	Langmuir isotherm			Freundlich isotherm		
	$K_L$ (mg/L)	$q_m$ (mg.g <sup>-1</sup> )	$R^2$	$P$ (mg.g <sup>-1</sup> )	$n$	$R^2$
T-CNF	0.036	185.2	0.997	32	3.91	0.89
T-CNF/SA	0.144	216.4	0.999	49.9	3.51	0.79

Freundlich isotherm models are displayed in Table 2. At 500 ppm MB content, the amount of MB dye removed increases from 177 mg.g<sup>-1</sup> to 214 mg.g<sup>-1</sup> for T-CNF and T-CNF/SA (Fig. 5A). MB migrates more actively from the aqueous to solid phases when dye concentrations are higher, enhancing contact between MB and adsorbents.

In this study, Langmuir isotherms were established and showed a high correlation coefficient was obtained ( $R^2 > 0.99$  for T-CNF and T-CNF/SA). It can demonstrate clearly that MB adsorbed on T-CNF and T-CNF/SA formed a monolayer by interacting directly with energetically equivalent adsorption sites (Table 2). Furthermore, from Langmuir isotherm modeling, the maximum MB adsorption capacity was

determined from T-CNF and T-CNF/SA was 185.2 mg.g<sup>-1</sup> and 216.4 mg.g<sup>-1</sup>, respectively.

### 3.5 Desorption Data

Adsorbents are extremely important in the industrial field, as they can be reused again and again. Figure 6 shows the results of repeated adsorption/desorption cycles of T-CNF and T-CNF/SA. Regeneration of the T-CNF and T-CNF/SA with 0.01 M HCl resulted in a slight decrease in adsorption capacity from 98 to 93 after the fourth cycle. Finally, T-CNF/SA often used as dye adsorbents for removing cationic dyes because they can be regenerated. The loss of adsorption



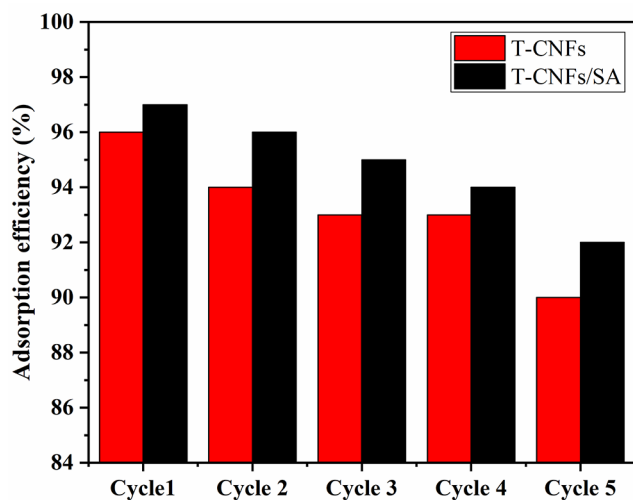


**Fig. 6** A reusability study of T-CNF and T-CNF/SA nanocomposite for MB adsorption

capacity after regeneration of T-CNF/SA nanocomposite with methylene blue dye can be attributed to several factors. Firstly, the regeneration process may cause damage to the nanocomposite structure, resulting in a decrease in its surface area and pore size. This can reduce the accessibility of the active sites on the nanocomposite surface, thereby reducing its adsorption capacity. Secondly, the regeneration process may also remove some of the functional groups on the surface of the nanocomposite, which are responsible for adsorbing the methylene blue dye. This can reduce the number of active sites available for adsorption and result in a loss of adsorption capacity. Finally, the regeneration process may also result in a decrease in the nanocomposite’s hydrophilicity, which can reduce its affinity for polar molecules such as methylene blue. This can also contribute to a loss of adsorption capacity.

A comparison between T-CNF/SA nanocomposite with others several adsorbents was summarized and documented in Table 3. The present data showed that T-CNF/SA nanocomposite had effective MB dye adsorption compared with various sustainable materials as report in the literatures.

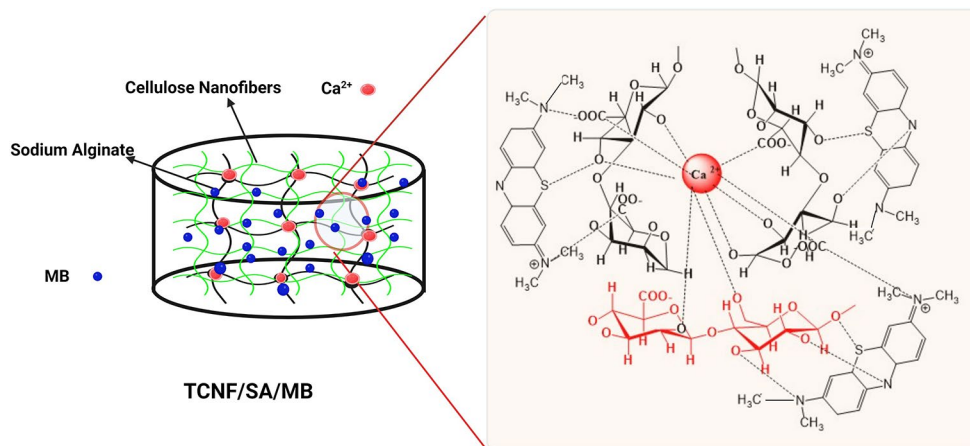
### 3.6 The Proposed Mechanism of the T-CNF and SA with Methylene Blue

The proposed mechanism of the prepared nanocomposite between T-CNF and SA with calcium chloride (CaCl<sub>2</sub>) involves the formation of ionic and electrostatic interactions between the carboxylate groups on the surface of the T-CNF and SA and the Ca<sup>2+</sup> ions, as seen in Fig. 7. This interaction leads to the formation of a nanocomposite material, which is stabilized by allowing the nanocomposite to incubate in a CaCl<sub>2</sub> solution for a specific period. The mechanism of adsorption of T-CNF/SA nanocomposite with methylene

**Table 3** MB dyes adsorption capacities of different modified nanocellulose

Adsorbent	pH	q <sub>max</sub> (mg.g <sup>-1</sup> )	Langmuir		Freundlich		Ref		
			Q <sub>max</sub> (mg.g <sup>-1</sup> )	K <sub>L</sub> (L.mg <sup>-1</sup> )	R <sup>2</sup>	P			
T-CNF	7	180	185.2	-	0.997	32	0.89	This work	
T-CNF/SA	7	218	216.4	-	0.999	49–9	0.79	This work	
Unmodified CNFs from Kenaf	9	100	122	0.178	0.996	12.8	0.85	[50]	
TEMPO-periodate-chlorite oxidation of CNFs	7	-	502	23.2	0.989	64	0.5	[24]	
Cellulose nanocrystals /Alginate hydrogel	-	256.4	256.4	0.002	0.998	1.54	1.931	0.988	[51]
CNF/carbon nanotubes hybrid	-	-	1178.5	0.11	0.985	364.2	4.984	0.892	[52]
TEMPO-Oxidized CNFs/ Graphene	-	227.2	151.51	0.0365	0.995	34.32	0.256	0.954	[53]
Carboxylation Cellulose nanocrystals	6–9	233	-	-	-	-	-	-	[54]
Chitosan-g-poly(acrylic acid) composite (5 wt% Cellulose nanocrystals)	7	79	101.2	0.019	0.974	-	-	-	[55]
Bio-Based Sodium Alginate/Lignin Composite	6	1968	2074	0.139	0.999	-	-	-	[56]
SA/MMT	-	254.3	-	-	-	-	-	-	[57]
	-	599.94	-	-	-	-	-	-	[58]

**Fig. 7** The proposed mechanism of adsorption of T-CNF/SA nanocomposite with methylene blue



blue involves several steps. First, the nanocomposite is introduced into a solution containing methylene blue. The methylene blue molecules diffuse into the nanocomposite, where they interact with the functional groups on the surface of the hydrogel. The functional groups on the surface of T-CNF/SA nanocomposite, such as hydroxyl and carboxyl groups, can form hydrogen bonds, electrostatic interactions, and van der Waals forces with methylene blue molecules. These interactions cause the methylene blue molecules to be adsorbed onto the surface of the nanocomposite as seen in Fig. 7.

## 4 Conclusion

TEMPO oxidized cellulose nanofibers (T-CNF) were successfully prepared by mechanical defibrillation using Masuko grinders with diameters in the range of 5 to 20 nm. The T-CNF/SA.

a nanocomposite was further characterized by SEM, TEM, FTIR rheology and XRD to understand the mechanism of formation of crosslinked nanocomposite. T-CNF/SA nanocomposite showed improved absorption capabilities of methylene blue from aqueous solution compared to T-CNF. Langmuir isotherms were found to better describe the adsorption process more than Freundlich isotherms, and it turned out that the maximum absorption capacity of the nanocomposite is  $216.4 \text{ mg} \cdot \text{g}^{-1}$  for methylene blue dye. The results indicate clearly that the T-CNF/SA nanocomposite is sustainable, environmentally friendly and sufficient as an adsorbent for the removal of dyes in industrial and environmental applications.

**Author Contribution** The authors of this article and their contribution to this work are equal contributions.

**Funding** No funding is available.

**Data Availability** The research data associated with a paper is available,

## Declarations

**Conflict of Interest** The authors declare no conflict of interest. Ramzi Khiari is Guest Editor of the Special Issue “Lignocellulose at multi-scale: preparation characterization.”

## References

1. Fiol N, Vásquez MG, Pereira M, Tarrés Q, Mutjé P, Delgado-Aguilar M (2019) TEMPO-oxidized cellulose nanofibers as potential Cu(II) adsorbent for wastewater treatment. *Cellulose* 26:903–916. <https://doi.org/10.1007/s10570-018-2106-7>
2. Dai L, Zhu W, He L, Tan F, Zhu N, Zhou Q, He M, Hu G (2018) Calcium-rich biochar from crab shell: an unexpected super adsorbent for dye removal. *Bioresour Technol* 267:510–516. <https://doi.org/10.1016/j.biortech.2018.07.090>
3. Jiao C, Li T, Wang J, Wang H, Zhang X, Han X, Du Z, Shang Y, Chen Y (2020) Efficient removal of dyes from aqueous solution by a porous sodium Alginate/gelatin/graphene Oxide Triple-network Composite Aerogel. *J Polym Environ* 28:1492–1502. <https://doi.org/10.1007/s10924-020-01702-1>
4. Song W, Gao B, Xu X, Xing L, Han S, Duan P, Song W, Jia R (2016) Adsorption-desorption behavior of magnetic amine/Fe<sub>3</sub>O<sub>4</sub> functionalized biopolymer resin towards anionic dyes from wastewater. *Bioresour Technol* 210:123–130. <https://doi.org/10.1016/j.biortech.2016.01.078>
5. Huang H, Liu J, Zhang P, Zhang D, Gao F (2017) Investigation on the simultaneous removal of fluoride, ammonia nitrogen and phosphate from semiconductor wastewater using chemical precipitation. *Chem Eng J* 307:696–706. <https://doi.org/10.1016/j.cej.2016.08.134>
6. Yagub MT, Sen TK, Afroze S, Ang HM (2014) Dye and its removal from aqueous solution by adsorption: a review. *Adv Colloid Interface Sci* 209:172–184. <https://doi.org/10.1016/j.cis.2014.04.002>
7. Yang Y, Zhao B, Tang P, Cao Z, Huang M, Tan S (2014) Flexible counter electrodes based on nitrogen-doped carbon aerogels with tunable pore structure for high-performance dye-sensitized solar cells. *Carbon N Y* 77:113–121. <https://doi.org/10.1016/j.carbon.2014.05.012>
8. Hassan M, Zeid REA, Abou-Elseoud WS, Hassan E, Berglund L, Oksman K (2019) Effect of unbleached rice straw cellulose nanofibers on the properties of polysulfone membranes, *Polymers (Basel)*. <https://doi.org/10.3390/polym11060938>

9. Hassan E, Hassan M, Abou-zeid R, Berglund L, Oksman K (2017) Use of bacterial cellulose and crosslinked cellulose nanofibers membranes for removal of oil from oil-in-water emulsions. *Polym (Basel)* 9. <https://doi.org/10.3390/polym9090388>
10. Mohan D, Kumar H, Sarswat A, Alexandre-Franco M, Pittman CU (2014) Cadmium and lead remediation using magnetic oak wood and oak bark fast pyrolysis bio-chars. *Chem Eng J* 236:513–528. <https://doi.org/10.1016/j.cej.2013.09.057>
11. El Samrani AG, Lartiges BS, Villieras F (2008) Chemical coagulation of combined sewer overflow: heavy metal removal and treatment optimization. *Water Res* 42:951–960. <https://doi.org/10.1016/j.watres.2007.09.009>
12. Wang L (2009) Aqueous organic dye discoloration induced by contact glow discharge electrolysis. *J Hazard Mater* 171:577–581. <https://doi.org/10.1016/j.jhazmat.2009.06.037>
13. Barquist K, Larsen SC (2010) Chromate adsorption on bifunctional, magnetic zeolite composites. *Microporous Mesoporous Mater* 130:197–202. <https://doi.org/10.1016/j.micromeso.2009.11.005>
14. Salama A (2016) Functionalized hybrid materials assisted organic dyes removal from aqueous solutions. *Environ Nanotechnol Monit Manag* 6:159–163. <https://doi.org/10.1016/j.enmm.2016.10.003>
15. Hassan ML, Fadel SM, Abouzeid RE, Abou Elseoud WS, Hassan EA, Berglund L, Oksman K (2020) Water purification ultra-filtration membranes using nanofibers from unbleached and bleached rice straw. *Sci Rep* 10:1–9. <https://doi.org/10.1038/s41598-020-67909-3>
16. Nan Y, Gomez-Maldonado D, Iglesias MC, Whitehead DC, Peresin MS (2023) Valorized soybean hulls as TEMPO-oxidized cellulose nanofibril and polyethylenimine composite hydrogels and their potential removal of water pollutants. *Cellulose* 92:83–91. <https://doi.org/10.1007/s10570-023-05086-y>
17. Wang Q, Liu S, Chen H, Liu J, Zhu Q (2022) TEMPO-oxidized cellulose beads for cationic dye adsorption, *BioResources*. 176056–6066. <https://doi.org/10.15376/biores.17.4.6056-6066>
18. Batmaz R, Mohammed N, Zaman M, Minhas G, Berry RM, Tam KC (2014) Cellulose nanocrystals as promising adsorbents for the removal of cationic dyes. *Cellulose* 21:1655–1665. <https://doi.org/10.1007/s10570-014-0168-8>
19. Abdullah AH, Yasin SA, Abdullah SM, Khalaf MY, Saeed IA (2022) A kinetic and isotherm study on removing methylene blue from aqueous solutions by oxidized cellulose nanostructure. *Emergent Mater* 5:1199–1212. <https://doi.org/10.1007/s42247-022-00397-5>
20. Abdelaziz MA, Owda ME, Abouzeid RE, Alaysuy O, Mohamed EII (2023) Kinetics, isotherms, and mechanism of removing cationic and anionic dyes from aqueous solutions using chitosan/magnetite/silver nanoparticles. *Int J Biol Macromol* 225:1462–1475. <https://doi.org/10.1016/j.ijbiomac.2022.11.203>
21. Abou-Zeid RE, Kamal KH, Abd El-Aziz ME, Morsi SM, Kamel S (2021) Grafted TEMPO-oxidized cellulose nanofiber embedded with modified magnetite for effective adsorption of lead ions. *Int J Biol Macromol* 167:1091–1101. <https://doi.org/10.1016/j.ijbiomac.2020.11.063>
22. Georgouvelas D (2022) Modified and hybrid cellulose-based materials for water purification,
23. Hassan ML, Abou-Zeid RE, Fadel SM, El-Sakhawy M, Khiari R (2014) Cellulose nanocrystals and carboxymethyl cellulose from olive stones and their use to improve paper sheets properties. *Int J Nanoparticles* 7:261–277. <https://doi.org/10.1504/ijnp.2014.067613>
24. Abou-Zeid RE, Salama A, Al-Ahmed ZA, Awwad NS, Youssef MA (2020) Carboxylated cellulose nanofibers as a novel efficient adsorbent for water purification. *Cellul Chem Technol* 54:237–245. <https://doi.org/10.35812/CELLULOSECHEMTECHNOL.2020.54.25>
25. Abou-Zeid RE, Dacrory S, Ali KA, Kamel S (2018) Novel method of preparation of tricarboxylic cellulose nanofiber for efficient removal of heavy metal ions from aqueous solution. *Int J Biol Macromol* 119:207–214. <https://doi.org/10.1016/j.ijbiomac.2018.07.127>
26. Abouzeid RE, Khiari R, El-Wakil N, Dufresne A (2019) Current state and New Trends in the Use of Cellulose Nanomaterials for Wastewater Treatment. *Biomacromolecules* 20:573–597. <https://doi.org/10.1021/acs.biomac.8b00839>
27. Rocher V, Siaugue JM, Cabuil V, Bee A (2008) Removal of organic dyes by magnetic alginate beads. *Water Res* 42:1290–1298. <https://doi.org/10.1016/j.watres.2007.09.024>
28. Wang L, Shelton RM, Cooper PR, Lawson M, Triffitt JT, Barralet JE (2003) Evaluation of sodium alginate for bone marrow cell tissue engineering. *Biomaterials* 24:3475–3481. [https://doi.org/10.1016/S0142-9612\(03\)00167-4](https://doi.org/10.1016/S0142-9612(03)00167-4)
29. Pettignano A, Tanchoux N, Cacciaguerra T, Vincent T, Bernardi L, Guibal E, Quignard F (2017) Sodium and acidic alginate foams with hierarchical porosity: Preparation, characterization and efficiency as a dye adsorbent. *Carbohydr Polym* 178:78–85. <https://doi.org/10.1016/j.carbpol.2017.09.022>
30. Abou-Zeid RE, Awwad NS, Nabil S, Salama A, Youssef MA (2019) Oxidized alginate/gelatin decorated silver nanoparticles as new nanocomposite for dye adsorption. *Int J Biol Macromol* 141:1280–1286. <https://doi.org/10.1016/j.ijbiomac.2019.09.076>
31. Fiol N, Poch J, Villaescusa I (2004) Chromium (VI) uptake by grape stalks wastes encapsulated in calcium alginate beads: equilibrium and kinetics studies. *Chem Speciat Bioavailab* 16:25–33. <https://doi.org/10.3184/095422904782775153>
32. Abouzeid RE, Khiari R, Ali KA (2022) Activated Charcoal/Alginate nanocomposite beads for efficient adsorption of the Cationic Dye Methylene Blue: kinetics and equilibrium. *Chem Afr* 178:485–493. <https://doi.org/10.1007/s42250-022-00560-9>
33. Sehaqui H, Zhou Q, Ikkala O, Berglund LA (2011) Strong and tough cellulose nanopaper with high specific surface area and porosity. *Biomacromolecules* 12:3638–3644. <https://doi.org/10.1021/bm2008907>
34. Lu P, Liu X, Liu X, Wu M (2018) Preparation of Self-supporting Bagasse Cellulose Nanofibrils Hydrogels Induced by Zinc Ions. *Nanomaterials* 8:800. <https://doi.org/10.3390/nano8100800>
35. Saito T, Kimura S, Nishiyama Y, Isogai A (2007) Cellulose nanofibers prepared by TEMPO-mediated oxidation of native cellulose. *Biomacromolecules* 8:2485–2491. <https://doi.org/10.1021/bm0703970>
36. Gurgel LVA, Júnior OK, de Gil RP, Gil LF (2008) Adsorption of Cu(II), cd(II), and pb(II) from aqueous single metal solutions by cellulose and mercerized cellulose chemically modified with succinic anhydride. *Bioresour Technol* 99:3077–3083. <https://doi.org/10.1016/j.biortech.2007.05.072>
37. Abouzeid RE, Khiari R, Beneventi D, Dufresne A (2018) Biomimetic Mineralization of Three-Dimensional Printed Alginate/TEMPO-Oxidized Cellulose Nanofibril Scaffolds for Bone Tissue Engineering. *Biomacromolecules*. 194442–4452. <https://doi.org/10.1021/acs.biomac.8b01325>
38. Onyianta AJ, Dorris M, Williams RL (2018) Aqueous morpholine pre-treatment in cellulose nanofibril (CNF) production: comparison with carboxymethylation and TEMPO oxidation pre-treatment methods. *Cellulose* 25:1047–1064. <https://doi.org/10.1007/s10570-017-1631-0>
39. Abbott AP, Bell TJ, Handa S, Stoddart B (2006) Cationic functionalisation of cellulose using a choline based ionic liquid analogue. *Green Chem* 8:784. <https://doi.org/10.1039/b605258d>
40. Abou-Zeid RE, Hassan EA, Bettaieb F, Khiari R, Hassan ML (2015) Use of Cellulose and Oxidized Cellulose Nanocrystals from Olive Stones in Chitosan Bionanocomposites, *J. Nanomater*. <https://doi.org/10.1155/2015/687490>

41. Nascimento DM, Nunes YL, Figueirêdo MCB, de Azeredo HMC, Aouada FA, Feitosa JPA, Rosa MF, Dufresne A (2018) Nanocellulose nanocomposite hydrogels: technological and environmental issues. *Green Chem* 20:2428–2448. <https://doi.org/10.1039/C8GC00205C>
42. Kim H, Song JE, Kim HR (2021) Comparative study on the physical entrapment of soy and mushroom proteins on the durability of bacterial cellulose bio-leather. *Cellulose* 28:3183–3200. <https://doi.org/10.1007/s10570-021-03705-0>
43. Liu L, Wan Y, Xie Y, Zhai R, Zhang B, Liu J (2012) The removal of dye from aqueous solution using alginate-halloysite nanotube beads. *Chem Eng J* 187:210–216. <https://doi.org/10.1016/j.cej.2012.01.136>
44. Lezehari M, Basly JP, Baudu M, Bouras O (2010) Alginate encapsulated pillared clays: removal of a neutral/anionic biocide (pentachlorophenol) and a cationic dye (safranin) from aqueous solutions. *Colloids Surf Physicochem Eng Asp* 366:88–94. <https://doi.org/10.1016/j.colsurfa.2010.05.021>
45. Salama A, Hesemann P (2018) New N-guanidinium chitosan/silica ionic microhybrids as efficient adsorbent for dye removal from waste water. *Int J Biol Macromol* 111:762–768. <https://doi.org/10.1016/j.ijbiomac.2018.01.049>
46. Liu Z, Zhang FS (2009) Removal of lead from water using biochars prepared from hydrothermal liquefaction of biomass. *J Hazard Mater* 167:933–939. <https://doi.org/10.1016/j.jhazmat.2009.01.085>
47. Salama A, Hesemann P (2018) Synthesis of N-Guanidinium-Chitosan/Silica hybrid composites: efficient adsorbents for Anionic Pollutants. *J Polym Environ* 26:1986–1997. <https://doi.org/10.1007/s10924-017-1093-3>
48. Salama A, Shukry N, El-Sakhawy M (2015) Carboxymethyl cellulose-g-poly(2-(dimethylamino) ethyl methacrylate) hydrogel as adsorbent for dye removal. *Int J Biol Macromol* 73:72–75. <https://doi.org/10.1016/j.ijbiomac.2014.11.002>
49. Mohan D, Pittman CU, Bricka M, Smith F, Yancey B, Mohammad J, Steele PH, Alexandre-Franco MF, Gómez-Serrano V, Gong H (2007) Sorption of arsenic, cadmium, and lead by chars produced from fast pyrolysis of wood and bark during bio-oil production. *J Colloid Interface Sci* 310:57–73. <https://doi.org/10.1016/j.jcis.2007.01.020>
50. Chan CH, Chia CH, Zakaria S, Sajab MS, Chin SX (2015) Cellulose nanofibrils: a rapid adsorbent for the removal of methylene blue. *RSC Adv* 5:18204–18212. <https://doi.org/10.1039/c4ra15754k>
51. Mohammed N, Grishkewich N, Berry RM, Tam KC (2015) Cellulose nanocrystal–alginate hydrogel beads as novel adsorbents for organic dyes in aqueous solutions. *Cellulose* 22:3725–3738. <https://doi.org/10.1007/s10570-015-0747-3>
52. Yu Z, Hu C, Dichiara AB, Jiang W, Gu J (2020) Cellulose nanofibril/carbon nanomaterial hybrid aerogels for adsorption removal of cationic and anionic organic dyes. *Nanomaterials* 10. <https://doi.org/10.3390/nano10010169>
53. Hussain A, Li J, Wang J, Xue F, Chen Y, Bin Aftab T, Li D (2018) Hybrid Monolith of Graphene/TEMPO-Oxidized Cellulose Nanofiber as Mechanically Robust, Highly Functional, and Recyclable Adsorbent of Methylene Blue Dye. *J. Nanomater.* <https://doi.org/10.1155/2018/5963982>
54. Qiao H, Zhou Y, Yu F, Wang E, Min Y, Huang Q, Pang L, Ma T (2015) Effective removal of cationic dyes using carboxylate-functionalized cellulose nanocrystals. *Chemosphere* 141:297–303. <https://doi.org/10.1016/j.chemosphere.2015.07.078>
55. He X, Male KB, Nesterenko PN, Brabazon D, Paull B, Luong JHT (2013) Adsorption and desorption of methylene blue on porous carbon monoliths and nanocrystalline cellulose. *ACS Appl Mater Interfaces* 5:8796–8804. <https://doi.org/10.1021/am403222u>
56. Melo BC, Paulino FAA, Cardoso VA, Pereira AGB, Fajardo AR, Rodrigues FHA (2018) Cellulose nanowhiskers improve the methylene blue adsorption capacity of chitosan-g-poly(acrylic acid) hydrogel. *Carbohydr Polym* 181:358–367. <https://doi.org/10.1016/j.carbpol.2017.10.079>
57. Chen T, Liu H, Gao J, Hu G, Zhao Y, Tang X, Han X (2022) Efficient Removal of Methylene Blue by Bio-Based Sodium Alginate/Lignin Composite Hydrogel Beads. *Polymers (Basel)*. 142917. <https://doi.org/10.3390/polym14142917>
58. García A, Culebras M, Collins MN, Leahy JJ (2018) Stability and rheological study of sodium carboxymethyl cellulose and alginate suspensions as binders for lithium ion batteries. *J Appl Polym Sci* 135:46217. <https://doi.org/10.1002/app.46217>

**Publisher's Note** Springer Nature remains neutral with regard to jurisdictional claims in published maps and institutional affiliations.

Springer Nature or its licensor (e.g. a society or other partner) holds exclusive rights to this article under a publishing agreement with the author(s) or other rightsholder(s); author self-archiving of the accepted manuscript version of this article is solely governed by the terms of such publishing agreement and applicable law.